

Chemical Thermal Runaway Modeling of Lithium-Ion Batteries for Prediction of Heat and Gas Generation

Niklas Weber,* Sebastian Schuhmann, Jens Tübke, and Hermann Nirschl

Along with the increased usage of lithium-ion batteries and their development in energy densities, safety issues arise that have to be investigated. The most serious battery safety event is called thermal runaway. Herein, a chemical thermal runaway model with ten decomposition reactions is developed. It is coupled with thermal simulations in order to predict temperature curves as well as amount and composition of released gases during thermal runaway. Simulations are validated by thermal abuse experiments in an autoclave. Detailed temperature measurements and gas analysis are included. Simulations and experimental results prove to be in good agreement. The model is further applied to investigate thermal runaway behavior of cells with different energy densities.

1. Introduction

Due to the rising importance of energy storage, lithium-ion batteries have recently been in the focus of researchers around the world. Advances in battery active materials, especially cathode materials with high nickel content, have led to higher-energy densities, which is beneficial for mobile application.^[1] However, high-nickel-content cathodes come at the cost of lower thermal stability,^[2] making further investigations on safety risks necessary.

The most hazardous safety event of lithium-ion batteries is called thermal runaway. It is defined as the rapid and uncontrolled release of stored energy by decomposition reactions of battery components. Initiation of thermal runaway can occur for various reasons. They range from crush due to mechanical impact to external overheating to electrical reasons like internal or external short-circuit or over(dis)charging.^[3] Potential

consequences are heat release, mechanical rupture, gas release, fire, and explosion.^[4]

Because of these severe consequences, efforts have been made to model and simulate thermal runaway behavior in order to reduce the necessity of costly experiments. The first widely spread model for the degradation of anodes was developed in 1999 by Richard et al.^[5,6] They used calorimetric data for model parametrization, valid for the onset temperature region up to 200 °C.^[7] In 2001, MacNeil et al. used a similar calorimetric method to publish a degradation model for LCO cathodes.^[8] Hatchard et al. combined these models for simulation of full cells in overheating

conditions.^[9] Newer publications on this field^[10–14] often refer to these models and extend them to cover a wider field of application.

The aim of this work is to enable a quick evaluation of a battery's safety risk due to thermal runaway which can be applied on a highly flexible battery cell production for cells of various types, sizes, and shapes.^[15] Therefore, a numerical model for safety assessment of lithium-ion batteries is developed in this work.

The chemical model presented in this work takes a closer look on the decomposition reactions during thermal runaway. This allows the evaluation of generated heat and gas based on the battery cell composition, which is useful dimensioning safety measures such as safety vents and thermal barriers.

The developed model focuses on full cell simulations under thermal abuse conditions. Therefore, the chemical model is coupled with thermal simulations in order to obtain temperature curves and total heat release from the simulation results.

For validation, a test rig for thermal abuse of batteries was built. Pouch cells were brought to thermal runaway by heating them at a constant rate. Measurements of the temperature profiles during the thermal runaway process and the corresponding gas release are analyzed in order to validate the simulation framework.


2. Chemical Model Description

The chemical model is based on ten reactions that represent the decomposition of battery components such as solid–electrolyte interphase (SEI), anode and cathode active materials, conducting salt, and electrolyte solvent.

The anode active material of the battery cells under testing is lithiated graphite which is known to react with organic electrolyte solvent according to the following reaction^[16]

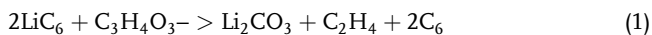
N. Weber, S. Schuhmann, H. Nirschl
Institute of Mechanical Process Engineering and Mechanics
Karlsruhe Institute of Technology
Straße am Forum 8, 76131 Karlsruhe, Germany
E-mail: niklas.weber@kit.edu

J. Tübke
Applied Electrochemistry
Fraunhofer Institute for Chemical Technology ICT
Joseph-von-Fraunhofer-Straße 7, 76327 Pfinztal, Germany

 The ORCID identification number(s) for the author(s) of this article can be found under <https://doi.org/10.1002/ente.202300565>.

© 2023 The Authors. Energy Technology published by Wiley-VCH GmbH. This is an open access article under the terms of the Creative Commons Attribution License, which permits use, distribution and reproduction in any medium, provided the original work is properly cited.

DOI: 10.1002/ente.202300565



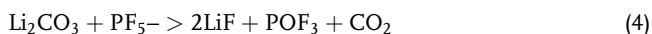
As a main electrolyte component, ethylene carbonate ($\text{C}_3\text{H}_4\text{O}_3$) is chosen as a representative solvent. Reaction Equation (1) is inhibited by the SEI which is formed on the surface of the active material as a product of reaction Equation (1) and other reactions.^[16] The SEI is mostly composed of organic and anorganic lithium salts. In this work only the anorganic lithium salts Li_2CO_3 , LiF, and Li_2O are considered. While this may lead to inaccuracies at modeling low-temperature SEI reactions, the influence of instable organic lithium salts can be neglected in higher-temperature regions, which are focused in this work as the inorganic lithium salts become the dominant surface species.^[17]

It is widely accepted that the inhibiting effect of the SEI on reaction Equation (1) at thermal runaway conditions is caused by electron tunneling as the limiting transport step.^[5,7,9,18] Thus, it can be modeled as an exponential factor, dependent on a dimensionless measure for SEI thickness z which acts as the tunneling barrier. Equation (5) describes the reaction rate for reaction Equation (1) according to Richard et al.^[5]

$$-\frac{dx_{\text{LiC}_6}}{dt} = x_{\text{LiC}_6} A_1 \exp\left(-\frac{E_1}{RT}\right) \exp(-z) \quad (2)$$

x_{LiC_6} is the mass fraction of anode active material, A_1 and E_1 are the pre-exponential factor and the activation energy according to Arrhenius theory, and R and T universal gas constant and temperature. Shurtz et al. analyzed differential scanning calorimetry (DSC) data published by various authors. They concluded that there is a limit for the described inhibition of the anode decomposition.^[7] This can be implemented in the model by limiting the dimensionless SEI thickness z to a maximum value z_{crit} .

Zhou et al. showed by DSC experiments that the amount of conducting salt LiP_6 largely affects the inhibition of the anode decomposition reaction Equation (1).^[19] The presence of LiP_6 leads into the formation of LiF on the anode surface via reactions Equation (3) and (4)^[20,21]



In accordance with this, Haik et al. detected with X-ray diffraction (XRD) measurements that LiF becomes the dominant species on the surface of anode active materials at temperatures above 120°C .^[17] Therefore, we regard LiF as the main inhibiting species for reaction Equation (1) and thus the dimensionless measure of SEI thickness z is directly coupled with the amount of produced LiF. The maximum value z_{crit} for the SEI thickness can be explained by the depletion of LiP_6 , limiting the formation of LiF. The relation between z and the amount of produced LiF is described by Equation (5)

$$z = z_{\text{crit}} \frac{x_{\text{LiF}}}{x_{\text{LiF,max}}} \frac{x_{\text{Electrolyte,0}}}{x_{\text{LiC}_6,0}} \quad (5)$$

x_{LiF} and $x_{\text{LiF,max}}$ are the current and the maximum mass fractions of LiF, and $x_{\text{Electrolyte,0}}$ and $x_{\text{LiC}_6,0}$ are the initial mass fractions of electrolyte and anode active material. Equation (5) is

formulated to conserve the empirically found value of $z_{\text{crit}} = 5.8$ ^[7] in case of equal initial mass of electrolyte and anode active material.

The maximum mass fraction of LiF $x_{\text{LiF,max}}$ is calculated based on the initial mass fraction of conducting salt $x_{\text{LiP}_6,0}$ according to Equation (6)

$$x_{\text{LiF,max}} = 3 x_{\text{LiP}_6,0} \frac{\widetilde{M}_{\text{LiF}}}{\widetilde{M}_{\text{LiPF}_6}} \quad (6)$$

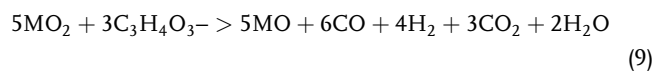
where $\widetilde{M}_{\text{LiF}}$ and $\widetilde{M}_{\text{LiPF}_6}$ are the respective molar masses and the factor 3 results from stoichiometry according to reactions Equation (3) and (4). As mentioned, at elevated temperatures, Li_2O becomes a notable species on the anode surface as well. It is formed by the decomposition of Li_2CO_3 , liberating CO_2 .^[17]



On the cathode side, the main decomposition reaction is the multistep phase transition of the metal oxide, which leads to the release of oxygen.^[8]

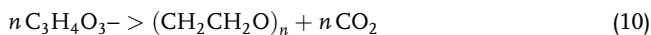
Bak et al. found by XRD measurements that layered metal oxide cathodes of the form Li_yMO_2 (where y is the degree of lithiation) transform to two different spinel-type oxides, LiM_2O_4 and M_3O_4 , in the first decomposition steps.^[22] The final transition step leads into a rock salt structure, chemically described as MO. M is a placeholder for the metal used in the metal oxide cathode. In the following, M will be used as an abbreviation for $\text{Ni}_{0.6}\text{Mn}_{0.2}\text{Co}_{0.2}$ as NMC622 was exclusively used as cathode active material in this work.

As simplification and due to the lack of detailed kinetic data on the multiple transition steps, these are regarded as a single-step cathode decomposition reaction under oxygen release. Liberated oxygen reacts with organic solvent in a partial or complete oxidation reaction^[23]



The electrolyte is composed of conducting salt LiPF_6 , a mixture of organic carbonates with ethylene carbonate as the main component and the additive vinylene carbonate. Vinylene carbonate is known to mitigate heat release of SEI decomposition at initiation temperatures around 100°C due to the formation of a more stable primary SEI.^[21] Both the conducting salt and the organic solvent on the other hand undergo decomposition reactions that significantly contribute to the thermal runaway behavior of the battery.

As mentioned, the organic solvent is a key reactant in the anode and cathode decomposition reactions. Furthermore, Lamb et al. showed that at $150\text{--}200^\circ\text{C}$ its organic structure decomposes through a ring opening, forming a polymeric product under gas release. Their gas analysis shows that CO_2 is the main gaseous product of this decomposition reaction.^[24] Therefore, the following chemical equation is used to account for solvent decomposition^[20]



$(\text{CH}_2\text{CH}_2\text{O})_n$ represents the various polymeric products. Zhou et al. performed further experimental studies on solvent decomposition, including kinetic studies.^[25] Besides, self-decomposition evaporation of organic solvent has to be regarded. The boiling point of ethylene carbonate is 248 °C, but Kriston et al. showed that solvent evaporation in an open system becomes significant at much lower temperatures starting at around 130 °C.^[11] As pouch cells are inclined to open due to overpressure during the heating process,^[26] they have to be considered an open system in the relevant temperature range. Thus, we introduced reaction Equation (11) to represent the solvent evaporation



The decomposition of conducting salt LiPF_6 according to reaction Equation (3) leads to the formation of other fluor-containing species. Besides the mentioned LiF formation, this is also the main source for emission of fluoric gases such as hydrogen fluoride. HF can be formed via reaction Equation (12)^[27,28]



Finally, the water–gas shift reaction is regarded for a more accurate prediction of the composition of released gas^[29]



All reactions used for chemical thermal runaway modeling in this work are summarized in **Table 1**. It also shows the reaction enthalpy for each reaction and the respective references.

For the solvent decomposition (reaction Equation (10)), no data on the reaction enthalpy could be found due to the undefined polymeric product. The reaction is assumed to be negligible in terms of heat release but still regarded as a contributor to gas release. For reaction Equation (3), (4), (7)–(13), reaction rates are calculated by power law kinetics (Equation (14)) with the reaction constant k_i according to the Arrhenius Equation (15):

$$r_i = k_i \prod_j x_j^{a_{j,i}} \quad (14)$$

$$k_i = A_i \exp\left(-\frac{E_i}{RT}\right) \quad (15)$$

In these equations, r_i is the reaction rate of reaction i , x_j and $a_{j,i}$ the mass fraction of species j and the according exponent for reaction i . Mass fractions of all species change according to Equation (16) where ν_{ij} is the stoichiometric coefficient.

$$\frac{dx_j}{dt} = \sum_i \nu_{ij} r_i \quad (16)$$

3. Experimental Section

3.1. Test Rig

The thermal runaway experiments were performed in a stainless steel DN400 T-piece with a total volume of 125 L (volume of test setup subtracted). The different pouch cells were placed between two aluminum blocks, which were heated by four heating cartridges with a total electrical power of 1200 W. The aluminum blocks were encased in fire protection panels to minimize the heat transfer to the outside. Furthermore, the aluminum blocks were wrapped in a fireproof insulation sheet to ensure a temperature difference between heating block and cell. This can be seen in **Figure 1** which shows an exploded view of the test rig.

During the experiments, the cell voltage, pressure, and the temperature at different spots were measured. Additionally, a low-budget gas sensor (MQ135 from AZ-Delivery), which is sensitive to CO , CO_2 , benzene, alcohol, smoke, as well as impurities in the air, was integrated to get extra information about the venting process during heating. Since the gas is a multiple mix, the calibration for absolute quantitative values is very complex. For this reason, we used the analog values of the sensor for the interpretation of the different stages during the experiment. The values varied between 0 and 5 V. The higher the value, the higher the amount of gases from the cell. Please notice that this allows only a relative view.

Since the cells blew up during heating, we wanted to detect the moment when the pressing force changed. Therefore, we used a small force-sensing resistor FSR (FSR05 from Arcol Ohmite) and

Table 1. Summary of chemical reactions with reaction enthalpies and references for reaction enthalpies.

Description	Chemical equation	Reaction Enthalpy [kJ mol ⁻¹]	References
Anode main reaction	$2\text{LiC}_6 + \text{C}_3\text{H}_4\text{O}_3 \rightarrow \text{Li}_2\text{CO}_3 + \text{C}_2\text{H}_4 + 2\text{C}_6$	-281.4	[7]
LiF formation	$\text{Li}_2\text{CO}_3 + \text{PF}_5 \rightarrow 2\text{LiF} + \text{POF}_3 + \text{CO}_2$	-77.1	[7,44,45]
Li_2O_2 formation	$\text{Li}_2\text{CO}_3 \rightarrow \text{Li}_2\text{O} + \text{CO}_2$	222.6	[7,46]
Cathode, full oxidation	$5\text{MO}_2 + \text{C}_3\text{H}_4\text{O}_3 \rightarrow 5\text{MO} + 3\text{CO}_2 + 2\text{H}_2\text{O}$	-201.5	[23,32]
Cathode, partial oxidation	$5\text{MO}_2 + 3\text{C}_3\text{H}_4\text{O}_3 \rightarrow 5\text{MO} + 6\text{CO} + 4\text{H}_2 + 3\text{CO}_2 + 2\text{H}_2\text{O}$	-105.5	[23,32]
Salt decomposition	$\text{LiPF}_6 \rightarrow \text{LiF} + \text{PF}_5$	84.27	[45]
Solvent decomposition	$n \text{C}_3\text{H}_4\text{O}_3 \rightarrow (\text{CH}_2\text{CH}_2\text{O})_n + n \text{CO}_2$		
Solvent evaporation	$\text{C}_3\text{H}_4\text{O}_3(l) \rightarrow \text{C}_3\text{H}_4\text{O}_3(g)$	60.8	[7]
HF formation	$\text{POF}_3 + 3\text{H}_2\text{O} \rightarrow 3\text{HF} + \text{H}_3\text{PO}_4$	-123.4	[44,47]
Water–gas shift	$\text{CO} + \text{H}_2\text{O} \rightleftharpoons \text{CO}_2 + \text{H}_2$	-41.2	[44]

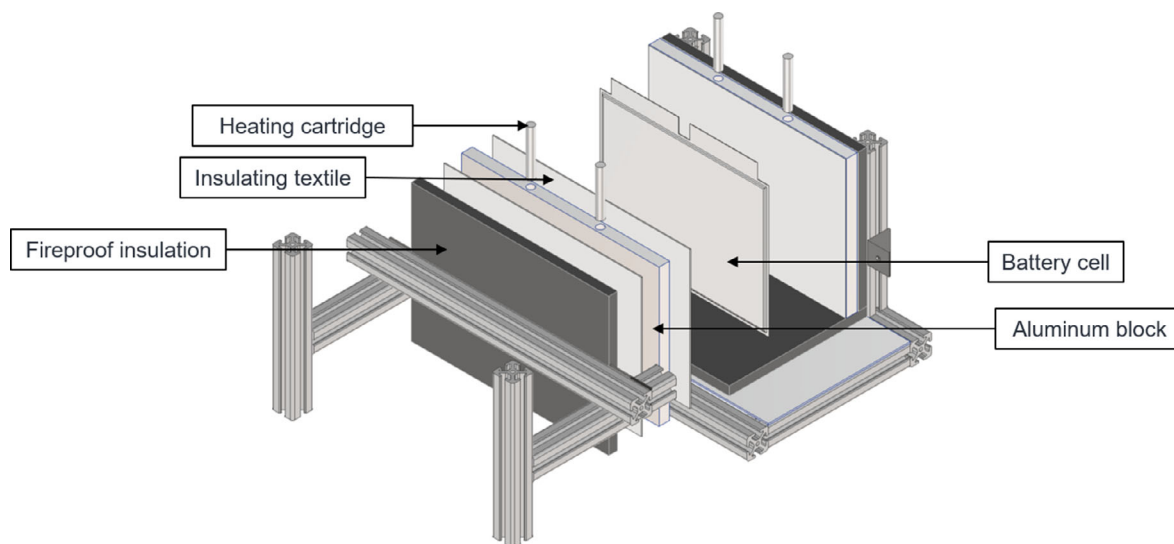


Figure 1. Exploded view of the test rig.

put it between the aluminum profile and the fire protection panel to detect changes in the pressing force. To keep things simple, we only used the relative change in values without calibration to detect the different stages of the experiment. For this purpose, we also used the analog values of sensors. The data of the MQ135 and the FSR sensor were logged with an Arduino Uno microcontroller.

All experiments were visually observed via a camera and a thermal imaging camera. Since the cell was located within the two heating blocks, the visual methods provide little information, but help interpret the measured data. This allows, for example, the moment of outgassing, smoke formation, or thermal runaway to be compared with the sensor data.

The test procedure is as follows.

1. Preparation of the experimental setup: The cell was weighed before m_0 and after m_1 each experiment to calculate the mass loss Δm from TR with the following equation.

$$\Delta m = \frac{m_0 - m_1}{m_0} \quad (17)$$

Please note that deviations from m_1 between the tests may occur due to the destroyed cell being removed from the test stand, as some parts may have fallen off when placed on the scale. Nevertheless, this method gave a good estimate for the mass loss.

2. The cell was placed between the two heating blocks and screwed hand tight. The setup was inserted in the autoclave and the screws were tightened with an impact wrench. Several thermoelements of type *K* (temperature range: between -200 and 1300 °C) were placed on different positions. Two thermoelements were placed on the front and backside of the cell. Another two thermoelements were mounted on the aluminum blocks. For the analysis of the temperature results the mean values of the cell and aluminum blocks were used.

3. Inerting of the autoclave: All experiments were performed under argon gas atmosphere. We used the swing pressure method to ensure a sufficient low oxygen concentration. The gas concentration can be estimated with following equation^[30]

$$c_n = c_i + (c_0 - c_i) \left(\frac{p_1}{p_2} \right)^{\frac{1}{k}} \quad (18)$$

c_n is the concentration after n cycles, c_0 the initial concentration (for oxygen 20.95% and nitrogen 78.00%), c_i the concentration of the gas component in the inert gas (argon gas with 0.004% rest oxygen), p_1 the lower pressure (1 atm), p_2 the higher pressure (we used 1.6 bar) and k the adiabatic exponent (for air $k = 1.47$). To keep the inert gas consumption as low as possible and still ensure sufficient inerting, we used ten cycles to get to an oxygen concentration below 1%. The first experiments showed good agreement between theory and praxis.

4. Heating ramp experiment: The aluminum blocks were heated with a heat ramp of 4 K min^{-1} until thermal runaway occurred. From the gas temperature and the pressure, the amount of gas could be calculated by the ideal gas law. After thermal runaway, we waited 15 min to take a gas sample with a 1 L Tedlar bag, which was brought to the gas analysis laboratory.

3.2. Gas Analysis

The gas from the Tedlar bag was analyzed by gas chromatography (GC) and the composition of the gases H_2 , O_2 , N_2 , methane, CO , ethane, CO_2 , ethene, ethyne, and propene was determined. A flame ionization detector (FID) and a thermal conductivity detector (TCD) were used for the GC.

3.3. Tested Battery Cells

For the experiments, pouch cells with the same chemistry but different capacities were used. The cells were produced by the Institute for Applied Materials - Energy Storage Systems (IAM-ESS) at Karlsruhe Institute of Technology (KIT). The cell's active materials were graphite on the anode side and NMC622 on the cathode side. A common commercial separator was used as well as LP30 electrolyte. Four different cell types with capacities of roughly 12, 15, 17, and 25 Ah were tested. Except for the 17 Ah

Table 2. Capacity and mass of all tested cells.

Label	Capacity [Ah]	Mass [g]
12.1	12.12	282.3
12.2	12.14	282.2
15.1	15.69	343.9
15.2	15.16	343.3
17.1	17.25	367.5
25.1	25.17	525.5
25.2	25.01	524.9

type cell, two cells of each type were tested for the sake of reproducibility. Due to a manufacturing error, only one 17 Ah type could be tested. Cell capacity and mass are listed in **Table 2** along with the labels that will be used in the following referring to the respective cells. In accordance with the simulations, all cells were tested at 100% state of charge (SOC).

4. Simulation Setup

4.1. Calculation of Battery Cell Properties

As an input for the chemical model, several cell properties have to be calculated. These include density, thermal conductivity, as well as the initial chemical composition of the battery cell. The cell manufacturer provides number and dimensions of anode, cathode and separator sheets, the volume of electrolyte, and the chemical composition of the used components. Porosity and thermal conductivity of individual sheets were measured at the Institute for Thermal Process Engineering (IVT) at KIT.

Due to their layered structure, the thermal conductivity of battery cells is anisotropic. We have to distinguish between thermal conductivity perpendicular to the sheets λ_{\perp} and thermal conductivity parallel to the sheets λ_{\parallel} . These two cases can be seen as series or parallel connections of thermal resistors. They are calculated according to Equation (19) and (20)^[31]

$$\lambda_{\perp} = \frac{\sum_i n_i s_i}{\sum_i \frac{n_i s_i}{\lambda_i}} \quad (19)$$

$$\lambda_{\parallel} = \frac{\sum_i n_i s_i \lambda_i}{\sum_i n_i s_i} \quad (20)$$

n_i , s_i , and λ_i are the number, thickness, and thermal conductivity of the different layers. For the calculation of averaged density and the initial chemical cell composition, the total volume V_i of each component is determined first. The electrolyte volume has been provided by the cell manufacturer; the volume of the porous layers is calculated by Equation (21)

$$V_i = n_i s_i A_i (1 - \varepsilon_i) \quad (21)$$

where A_i and ε_i are area and the porosity of layer i . Averaged density $\bar{\rho}$ and the initial mass fractions of all components x_i are then determined with Equation (22) and (23)

$$\bar{\rho} = \frac{\sum_i V_i \rho_i}{\sum_i V_i} \quad (22)$$

$$x_i = \frac{V_i \rho_i (1 - \gamma_i)}{\sum_j V_j \rho_j} \quad (23)$$

For the mass fractions of anode and cathode active material, we introduced γ_i which accounts for the binder and additive volume fraction in the electrodes. In addition, for the cathode active material, it has to be considered that even in a fully charged battery cell at 100% SOC the cathode is not completely delithiated. According to Shurtz et al., the degree of lithiation of a NMC622 cathode at 100% SOC is about 0.3^[32]; therefore, this value will be used for further calculations.

The electrolyte is mostly composed of organic solvent and conductive salt. Since the volume and the density of the electrolyte are given, the total mass is known and the mass of the individual electrolyte components can be calculated by the electrolyte composition provided by the manufacturer.

The remaining components, namely, the pouch bag, current collectors, separators, and electrode additives, are considered inert mass that does not take part in chemical reactions. **Table 3** shows the calculated properties of the cells under testing.

Due to the lack of high-temperature data of the cell's heat capacity, we set it to be 1300 J kg⁻¹ K⁻¹. This is above common literature data,^[9,33,34] but as Loges et al. proved, heat capacity significantly increases with rising temperature,^[33] which makes this a valid assumption for the relevant temperature region.

4.2. Thermal Simulation and Coupling with Chemical Model

For accurate representation of the experimental conditions, the entire test rig shown in Figure 1 was modeled in 3D and full thermal simulations are performed. **Table 4** lists the thermal properties of the insulations and the heater blocks. The data was provided by the manufacturers.

Table 3. Calculated battery cell properties.

Thermal data					
Cell type	λ_{\perp} in W m ⁻¹ K ⁻¹	λ_{\parallel} in W m ⁻¹ K ⁻¹	$\bar{\rho}$ in kg m ⁻³		
12 Ah	0.5740	23.388	2856.5		
15 Ah	0.5750	23.400	2807.9		
15 Ah	0.5755	23.404	2849.7		
25 Ah	0.5767	23.418	2710.8		
Initial mass fractions					
Cell type	Anode	Cathode	Solvent	Conducting salt	Inert
12 Ah	15.92%	27.62%	17.03%	2.32%	37.11%
15 Ah	15.95%	28.30%	17.44%	2.38%	35.93%
17 Ah	16.29%	29.13%	16.33%	2.23%	36.02%
25 Ah	16.14%	29.63%	18.28%	2.49%	33.46%

Table 4. Test rig thermal properties.

	Thermal conductivity [W m ⁻¹ K ⁻¹]	Heat capacity	Density	Thickness [cm]
Heating blocks	235	900 J kg ⁻¹ K ⁻¹	2700 kg m ⁻³	15
Fire protection	0.32	1100 J kg ⁻¹ K ⁻¹	1150 kg m ⁻³	15
Insulation sheets	0.06			0.13

The insulation sheets are modeled as thermal resistance, their heat capacity is neglected due to their low thickness. The heating cartridges are represented as local heat sources with heating power according to the experiments. The thermal simulations were coupled with the chemical model described in Section 2 by providing the local temperature distribution as an input for the calculation of reaction rates. For the thermal simulations, the chemical model acts as a heat source term dependent on the reaction rates of all reactions. As Equation (24) shows, the reaction rates r_i and the resulting volumetric heat source \dot{q} are linked via the reaction enthalpies $\Delta H_{r,i}$.

$$\dot{q} = \sum_i r_i \Delta H_{r,i} \quad (24)$$

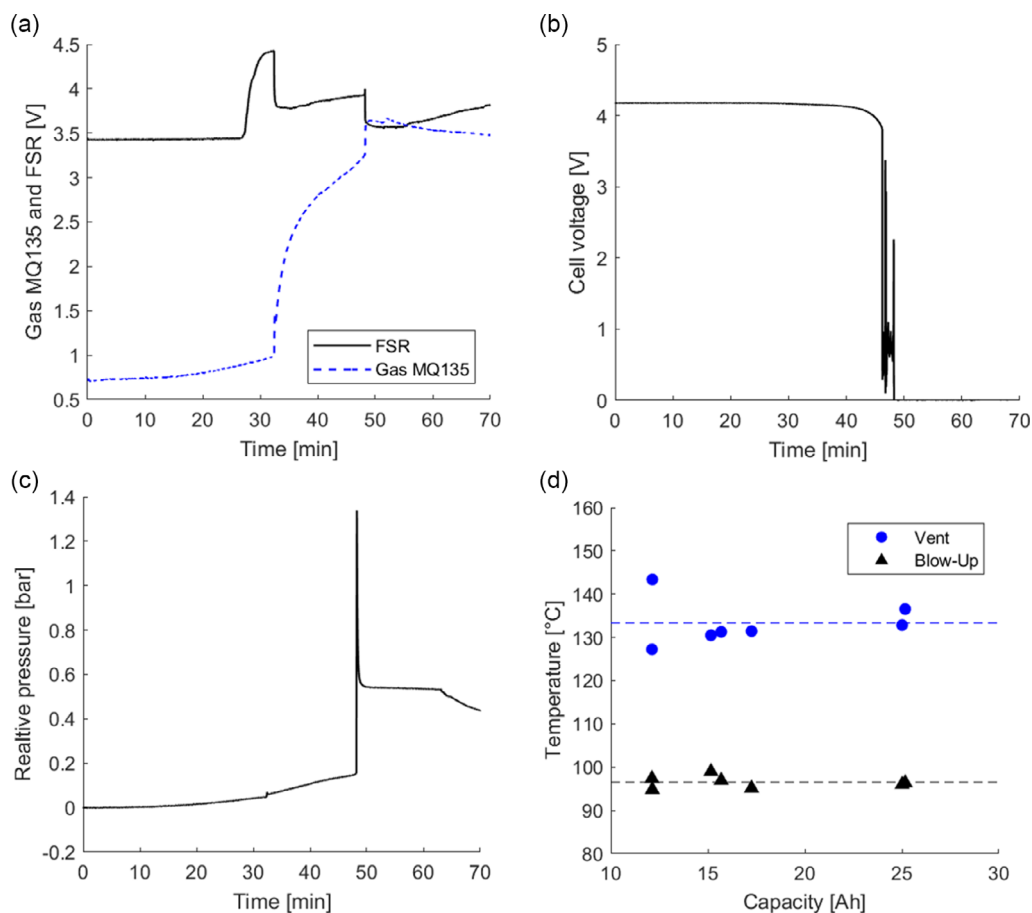


Figure 2. a) MQ135 and FSR sensor data for cell 25.1. b) Voltage of cell 25.1. c) Pressure development during experiment with cell 25.1. d) Comparison of blow-up and venting temperatures of all tested cells.

By combining thermal and chemical simulations, detailed results on temperature profiles of the battery cells during the thermal runaway process can be calculated. In addition, amount and species of released gases can be obtained from the composition data and compared with experimental results. For both thermal and chemical simulations, the open source software OpenFOAM was used.

5. Results and Discussion

In this section the simulation results are compared with the experimental data in terms of heat and gas generation for validation of the presented model. The validated model is then used to predict thermal runaway behavior of different cell types.

5.1. Experimental Observations

In this subsection, it is explained how additional sensor data helps to interpret the results of several events during thermal runaway experiments. In Figure 2a–c, the sensor data of the experiment with cell 25.1 are shown as an example.

The FSR sensor is used to get more details about the blow-up event during the experiments. Due to the inflation at $\approx 96.5^\circ\text{C}$,

the cell presses against the surrounding walls and the pressing force increases, which is measured with the FSR sensor. The blow-up of the cell was defined as an increase of the initial value $U_{\text{FSR},0}$ by 0.15 V. In the example in Figure 2a, $U_{\text{FSR},0}$ is 3.45 V, so the voltage of the blow-up event was calculated to be $U_{\text{FSR,Blow-Up}} = 3.60$ V.

The MQ135 sensor is useful to detect the venting event during the experiments. The analog value of the sensor changes significantly as soon as the gas leaves the cell. The derivation is used to determine the exact moment of the event and is defined in this work by 2 V min^{-1} .

Figure 2d shows the temperatures at which these events occur for all tested cells, determined with the described methods. The average temperatures, visualized with dashed lines, are $96.5 \text{ }^\circ\text{C}$ for the blow-up event and $133.3 \text{ }^\circ\text{C}$ for the venting event. For both events, there is little deviation from the average values and no notable influence of the cell capacity.

As Figure 2b,c shows, we further measured the cell voltage to detect the moment of the separator breakdown and the pressure inside the autoclave to calculate the amount of gas with the ideal gas law.

$$n_{\text{gas}} = \frac{pV}{RT_{\text{gas}}} \quad (25)$$

The gas temperature T_{gas} is measured at two different positions inside the autoclave, as T_{gas} fluctuates greatly. One position is next to the camera system and the other position is in front of the experimental setup. The gas is collected 15 min after thermal runaway to reach a sufficient state of equilibrium, and the average of the two values is calculated for the determination of the gas quantity n_{gas} . The gas volume V_{gas} is calculated at standard ambient temperature and pressure (SATP) conditions ($25 \text{ }^\circ\text{C}$ and 1 atm) with $V_{\text{m,gas}} = 24.465 \text{ L mol}^{-1}$.

$$V_{\text{gas}} = n_{\text{gas}} V_{\text{m,gas}} \quad (26)$$

Other useful data that can be obtained from the experiments is the mass loss of the cells during the experiments. As described in Section 3.1, the cells were weighed before and after the experiments. Table 5 displays the absolute and relative mass loss of all cells during the experiments.

The mass loss is about 9.59 g Ah^{-1} , which gives an average loss of 44.73%. These results are in good agreement with the values found by Hoelle et al.,^[35] where different thermal runaway experiments are compared.

Table 5. Mass loss of all tested cells.

Label	Mass loss [g]	Mass loss [%]
12.1	104.1	36.91%
12.2	95.6	33.87%
15.1	129.5	37.66%
15.2	106.3	30.96%
17.1	147.1	40.02%
25.1	310.6	59.11%
25.2	211.4	40.27%

5.2. Temperature Curves

Figure 3 shows the comparison of temperature curves obtained from experiments and simulation. In the experiments, the shown temperature curves were measured on the cell surface at the center. In simulations, the temperature was probed at the according positions. Four main stages can be observed. 1) In the first stage up to $96.5 \text{ }^\circ\text{C}$ is slowly heated according to the heating ramp defined for the experiment. Due to the low temperature, the chemical reactions hardly impact the heating of the battery cell. 2) Starting at around $96.5 \text{ }^\circ\text{C}$, a significant amount of gas is formed due to the onset of chemical reactions. This results in cell swelling, which can be detected with the FSR sensor, as shown in Section 5.1. It can also be visually observed with the camera, placed inside the autoclave. Besides that, this has an impact on the temperature curve as the cell heats faster than the intended heating rate. This is a consequence of the compression of the insulating sheets between the heater and the battery cell which lowers their thermal resistance. This behavior can only be seen in the experimental curves since the simulation model does not account for mechanical stress in the battery cell and the insulation material. As mentioned in Section 5.1, at around $133.3 \text{ }^\circ\text{C}$ the cell opens due to the internal pressure, releasing vent gases. At this point, the temperature drops due to the decompression of released gases. 3) In the further heating process, decomposition reactions intensify, leading into self-heating of the battery cell. At the onset temperature of rapid thermal runaway, the self-heating rate has come to a critical point. The consequence is a temperature rise of $300\text{--}400 \text{ }^\circ\text{C}$ within seconds which is characteristic for thermal runaway events. The peak temperature is reached when the reactive educts are depleted and therefore the chemical reactions come to a sudden halt. 4) After reaching the peak temperature, the cooling stage starts immediately. In the beginning, the cell cooling is dominated by the assimilation of the heating block temperature to the battery cell temperature, which results in a relatively quick temperature drop. After that it only cools due to heat loss to the gas surrounding the test rig, resulting in a significantly lower cooling rate.

The experimental temperature curves in Figure 3 confirm the results from the FSR and MQR135 sensors, shown in Section 5.1, that the cell capacity has no influence on the temperature of cell swelling and cell opening. As the internal pressure build-up due to gas production is not included in the simulation model, venting time and temperature cannot be compared to experiments.

The exact onset temperature of transition to rapid thermal runaway is hard to pinpoint. Therefore, we define as a criterion a self-heating rate of at least $20 \text{ }^\circ\text{C min}^{-1}$ over 2 s or more. Again, referring the onset temperature to the cell capacity does not show a clear trend and low variation overall. Except for cell 12.2, all cells transit to rapid thermal runaway at temperatures between 200 and $209 \text{ }^\circ\text{C}$ in the experiments. The simulations slightly overpredict the onset temperature, ranging from 209 to $214 \text{ }^\circ\text{C}$.

The temperature curve of cell 12.2 deviates strongly from all other tested cells and from the simulation results. This explains rupture in the test rig which occurs at the first venting event. After that the cell was thermally contacted properly with one of the heater blocks. Therefore it has the lowest onset and peak temperatures at 196.5 and $466 \text{ }^\circ\text{C}$ respectively.

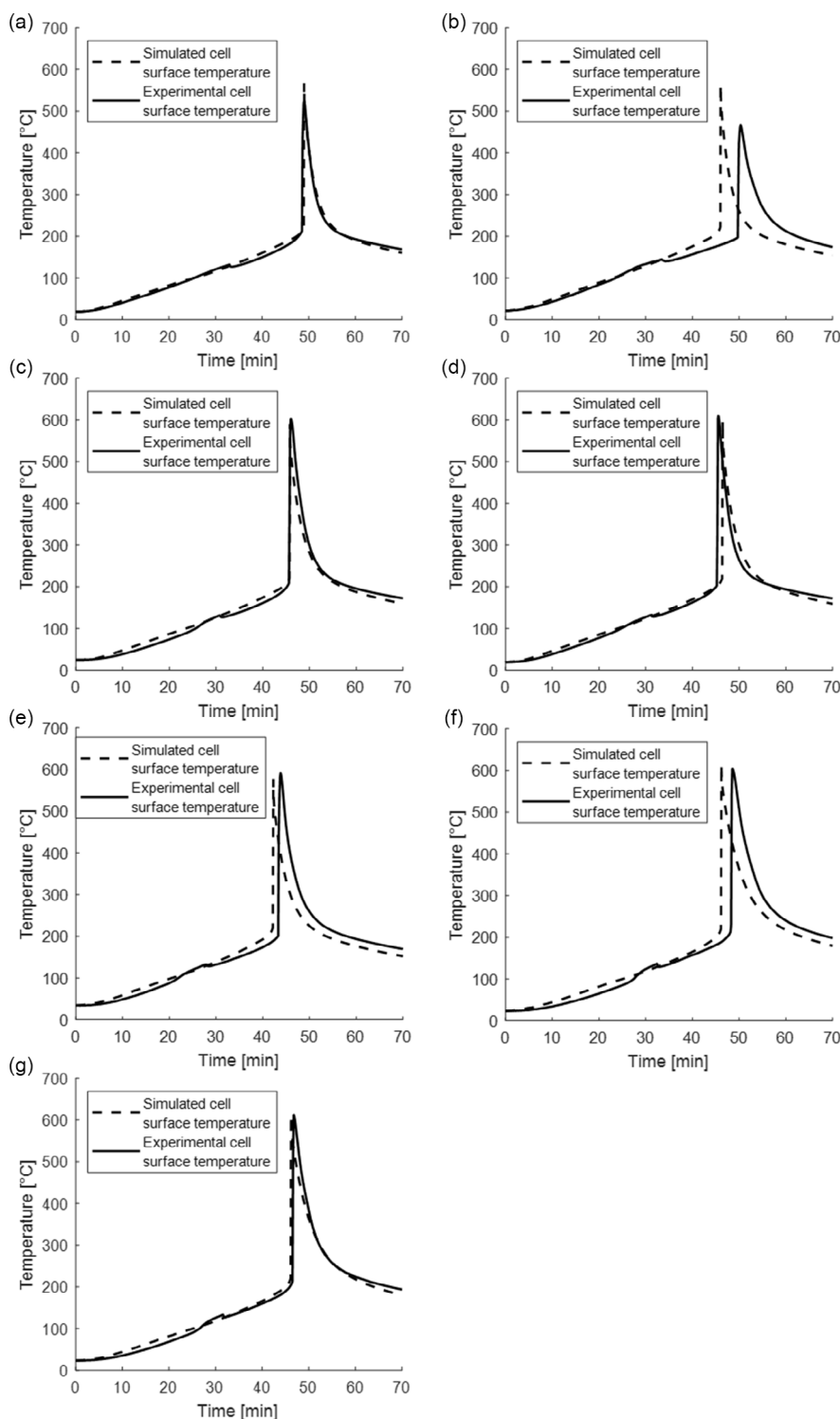


Figure 3. Comparison of experimental and simulated temperature curves for all experiments (cell labels as introduced in Table 2): a) 12.1, b) 12.2, c) 15.1, d) 15.2, e) 17.1, f) 25.1, and g) 25.2.

Figure 4 shows the peak temperatures on the cell surface measured during the experiments or obtained from the simulation results for all tested cells. All tested cells reach peak temperatures between 465 and 615 °C with a tendency that higher peak

temperatures are reached the bigger the cell is. However, there are several deviations from this behavior as cells 15.2 and 17.1 reach lower peak temperatures than cell 15.1 despite having a higher capacity.

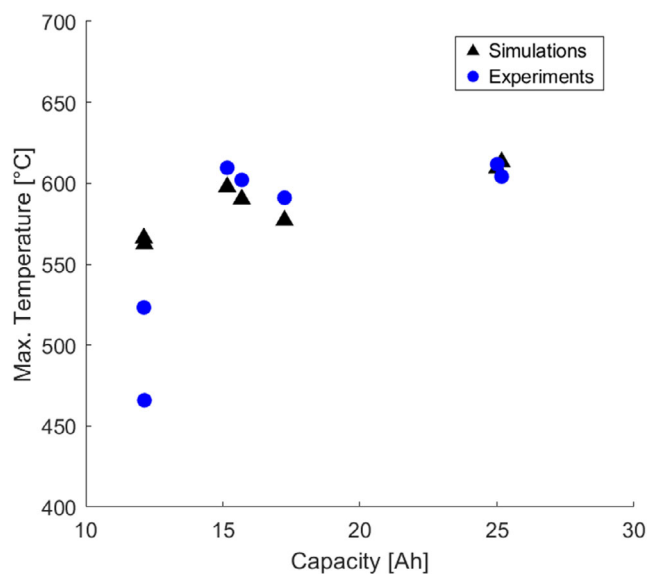


Figure 4. Comparison of simulated and experimental peak temperatures.

For cell 17.1 the deviation can be explained by the lower mass fraction of electrolyte (see Table 3). As the organic electrolyte is a main reactant in both anode and cathode decomposition reactions, its depletion leads into a significant diminution of heat release. Analysis of composition data in the simulations shows that a smaller fraction of active material undergoes decomposition reaction before depletion of the solvent compared to the other cells.

Despite their difference in capacity cells, 15.1 and 15.2 have the same internal build-up and therefore the same composition. The small deviation in peak temperature of 7 °C originates from slight differences in ambient temperature and heating conditions. Overall for all tested cells with a capacity of at least 15 Ah there is an excellent agreement in peak temperature between experiments and simulations with a maximum deviation of 15 °C. The 12 Ah type cells however show notable deviations of 42.9 and 96.6 °C.

5.3. Gas Release

Figure 5 shows the total amount released during the experiments compared to the simulations. In the experiments the amount of gas is calculated from pressure measurement as described in Section 5.1; in the simulations, it is obtained from the mass composition data. Referring the standard volume of released gas to cell capacity results in an average of 2.39 L Ah⁻¹ for the experiments and 2.79 L Ah⁻¹ for the simulations. The difference between simulations and experiments is explained by condensation of water and solvent, which are released in a gaseous state. Literature data with comparable experimental setups report around 1.5–2.5 L Ah⁻¹ for overheating tests on NMC cells.^[35–38] The reason for the relatively high amount of released gas in this work is the high initial electrolyte mass fraction compared to commercial cells^[39] as electrolyte solvent contributes to several gas-producing decomposition reactions (see Section 2).

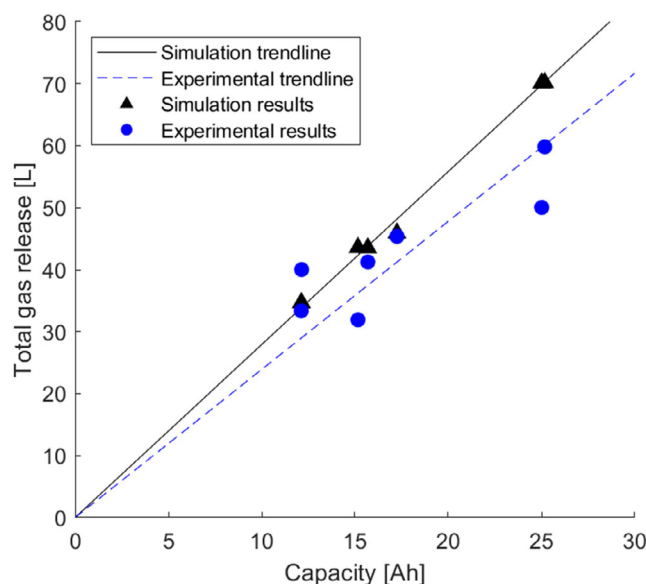


Figure 5. Simulated and experimental total amount of gas released for all cells.

Compared to simulation data, experimental gas release are scattered around the mean value (dashed line in Figure 5), ranging from 2.0 to 3.3 L Ah⁻¹ overall. Due to the chaotic nature of thermal runaway events, even identical cells show significant differences in gas release. Comparing the two 25 Ah cells, there is a 19.6% difference in the amount of released gas despite almost identical onset and peak temperatures. However, a similar scattering behavior was reported by Koch et al.^[36] and Hoelle et al.^[35] as well.

For the comparison of gas composition data, we used CO₂, CO, H₂, and hydrocarbons fractions, which are the main species released during thermal runaway.^[39] The simulations cannot cover the wide variance of released hydrocarbons. Therefore, the amount of different hydrocarbons is summed up and compared in a lump. The fractions of the named species are compared relative to each other.

Figure 6 shows the comparison of gas compositions for simulations and experiments. In accordance with literature results,^[35–37,39] CO₂ is the main released component for all cells except the 12 Ah type cells. It is produced by multiple decomposition reactions on the anode and the cathode side and by solvent self-decomposition (reactions Equation (4), (7)–(10)). On average, the gas analysis detected 40.8 Vol% CO₂ and the simulations averaged at 41.4 Vol% CO₂. H₂ and CO both evolve from partial oxidation of the electrolyte solvent (reaction Equation (9)). CO has an average volume fraction of 30.0 Vol% in the experiments and 27.0 Vol% in the simulations, while H₂ averaged at 18.8 and 17.4 Vol% respectively. Hydrocarbons with ethene as their main component mostly evolve as a product of the anode main decomposition reaction (Equation (1)). They were found with a fraction of 10.2 and 14.2 Vol% in the experiments and simulations respectively.

Again, the experimental results were found to scatter much more than the simulation results. Simulation results only show little differences between all cells due to their similar composition. On the other hand, the experimental gas analysis of

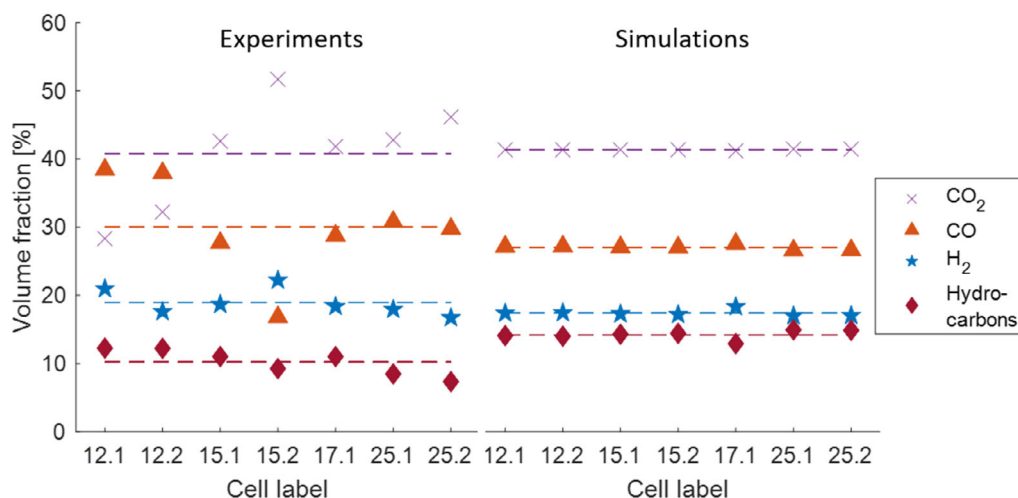


Figure 6. Experimental (left) and simulated (right) gas compositions. Dashed lines represent the average values.

both 12 Ah type cells results in a significantly below-average CO₂/CO ratio of 0.74 and 0.85, while cell 15.1 released gas with an above average CO₂/CO ratio of 3.07. Also, the experimental results show a slight tendency of decreasing hydrocarbon volume fraction that cannot be found in the simulations.

5.4. Cell Types

The validated model was then used to compare predicted thermal runaway behavior of different cell types, which differ in energy and power density. Given that the same cell chemistry is used, high-energy and high-power cells mainly differ in the thickness of electrode layers and electrode porosity.^[40,41] The values for electrode thickness and porosity were taken from Schmidt et al. who used an electrical model to optimize these data for different requirements in terms of energy and power density.^[42,43] Five different optimized cell types are considered in this work. For simplification, they will be labeled as type A, B, C, D, and E with respective energy densities of 558, 549, 522, 472, and 393 Wh L⁻¹.

With Equation (19)–(23) thermal conductivity, density and initial chemical composition were calculated. The results are displayed in **Table 6**.

According to Equation (19) and (20), thermal conductivity parallel to the sheets is dominated by the most conductive layers while thermal conductivity perpendicular to the sheets is dominated by the least conductive layers. Due to the low electrode thickness, high-power cells have more highly thermal conductive current collectors but also more separators with low thermal conductivity. This results in a relatively high thermal conductivity parallel to the sheets but low thermal conductivity perpendicular to the sheets compared to high energy cells.

Looking at the initial compositions, high-energy cells have higher mass fractions of active anode and cathode active material because of their higher electrode thickness. Due to the lower porosity, the electrolyte mass fraction is also lower.

Figure 7 shows the simulated temperature curves of the five cell types. It shows that the higher mass fraction of active material leads into a higher heat generation during the slow

Table 6. Calculated properties of the five modeled cell types.

Thermal data					
Cell type	λ_{\perp} in W m ⁻¹ K ⁻¹	λ_{\parallel} in W m ⁻¹ K ⁻¹	$\bar{\rho}$ in kg m ⁻³		
1	0.6689	12.829	2905.7		
2	0.6653	13.020	2898.3		
3	0.6182	18.144	2945.6		
4	0.5615	25.497	2983.3		
5	0.4974	36.185	3017.1		
Initial mass fractions					
Cell type	Anode	Cathode	Solvent	Conducting salt	Inert
1	21.51%	33.01%	14.33%	1.95%	29.20%
2	21.21%	32.96%	14.58%	1.99%	29.26%
3	19.10%	31.61%	14.28%	1.95%	33.06%
4	16.48%	28.73%	14.33%	1.95%	38.51%
5	13.16%	23.90%	14.65%	2.00%	46.29%

self-heating stage. The consequence is an earlier onset of rapid thermal runaway for high-energy cells, which is in accordance with results from Koch et al.^[36] For these cell types, the onset temperature ranges from 206.9 to 217.9 °C. This results in a difference in onset time of about 5 min between cell type A and E.

The peak temperatures of the five cell types show a rising trend with increasing energy density. However, there are slight deviations from that trend that can be explained with the varying initial mass fraction of electrolyte, which is a key reactant in multiple heat-releasing reactions. Overall, the peak temperatures range from 482 to 520 °C in the given setup.

The total amount of released gas shows a clear dependence on energy density as well. The higher-power cell type E has the highest specific gas release with 2.82 L Ah⁻¹ while energy cell type A releases the lowest amount of gas with 2.23 L Ah⁻¹.

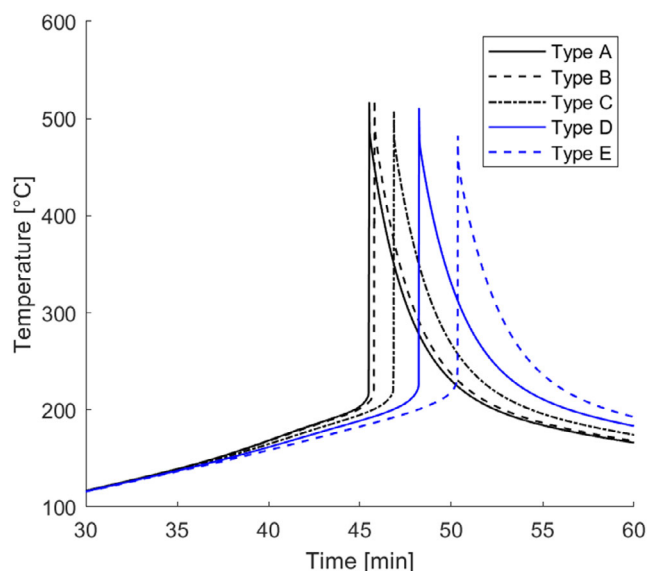


Figure 7. Simulated temperature curves of the five different cell types.

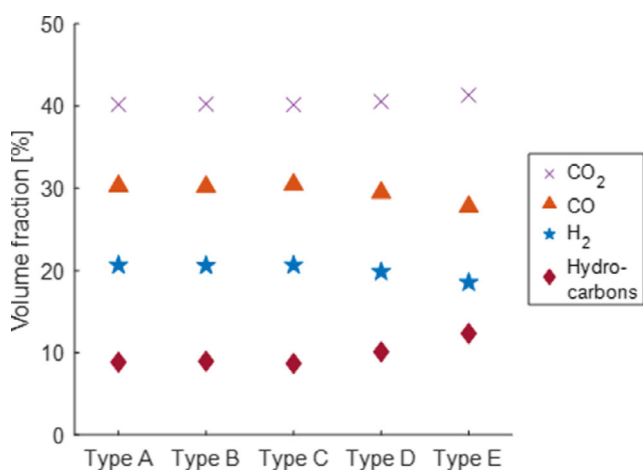


Figure 8. Simulated gas composition of the five different cell types.

The composition of released, shown in **Figure 8**, is found to be similar for the cell types A to C with about 40% CO₂, 30% CO, 21% H₂, and 9% hydrocarbons. The high-power cells D and E however release a higher fraction of hydrocarbons, which indicates a higher degree of decomposition on the anode side according to reaction Equation (1). Moreover, the CO₂/CO ratio is shifted more toward CO₂ compared to the high-energy cells. This is explained by the lower peak temperature which influences the equilibrium of the water–gas shift, according to reaction Equation (13).

6. Conclusion and Outlook

In this work, a chemical model is developed for the prediction of thermal runaway of lithium-ion batteries. Ten representative

reactions were presented to cover different stages from slow onset to rapid thermal runaway. It was shown how this model can be combined with a thermal simulation in order to predict temperature curves and gas release of battery cells under thermal runaway conditions.

The setup based on a chemistry solver also easily allows to refine the model for future works by adding further species and reactions for a more detailed representation of certain decomposition processes.

For validation, heating ramp experiments and simulation of cells with different capacities but same cell chemistry were compared. We showed how simple, additional sensor equipment can be used to detect important events during the thermal runaway process. It was found that there is no significant influence of cell capacity on the temperature of cell swelling (around 96.5 °C), venting (around 133.3 °C), and onset of rapid thermal runaway (around 200–209 °C). Peak temperature however showed a clear dependence on cell capacity and ranged from 466 to 615 °C overall. The simulation model was able to predict the peak temperature of all cells with a capacity of 15 Ah or more within a range of 15 °C and the onset temperatures within a range of 10 °C.

The total amount of released gases was measured to be 2.39 L Ah⁻¹ in the experiments and 2.79 L Ah⁻¹ in the simulations on average. The model further proved to be able to predict the composition of the main released gas components within a small margin. This helps in risk assessment of fire and further heat release due to flammability of released gaseous species (H₂, CO, hydrocarbons), if thermal runaway occurs in a noninert environment. Moreover, potential hazards due to the release of toxic gases (CO, HF) can be evaluated.

Further, it was shown how the model takes different cell types with various energy and power densities into account. The simulations show that cells with higher energy density have a lower onset temperature and a higher peak temperature. The specific amount of released gases on the other side was found to be lower than in case of high-energy cells. The composition of released gases showed a higher fraction of hydrocarbons and a higher CO₂/CO ratio for the high-power cells but a lower fraction of H₂.

The developed model is believed to be a powerful tool for dimensioning safety measures of battery packs. Applying the model on simulation of multiple cells or battery modules can give valuable insight on heat and gas production during hazardous events and may help to decide on counter measures. This will be in the focus of future works.

Acknowledgements

This work was funded by the Baden-Württemberg Ministry of Science, Research and the Arts, within the project “AgiloBat” as part of the Innovation Campus Mobility of the Future. The authors would like to thank the Fraunhofer Institute for Chemical Technology (ICT), Pfinztal, Germany, for support in developing and conducting the battery test experiments and gas analysis. During the development of the battery tests, we received special support from Franziska Klein, Markus Hagen, Jens Froberg, Thomas Bayha, Patrik Fanz, Thomas Berger, and Brahim Bet. The authors would also like to thank Michael Abert and Kevin Gneuppel for their expertise and realization of the gas analyses. The authors further thank Robert Löwe and Olivia Wiegand (both Institute for Applied Materials - Energy Storage Systems, KIT) for producing battery cells for the experiments and Julia

Gandert (Institute for Thermal Process Engineering, KIT) for measuring and providing thermal data on the electrode and separator sheets.
Open Access funding enabled and organized by Projekt DEAL.

Conflict of Interest

The authors declare no conflict of interest.

Data Availability Statement

The data that support the findings of this study are available from the corresponding author upon reasonable request.

Keywords

chemical modeling, lithium-ion batteries, thermal abuse, thermal runaway

Received: May 25, 2023
Revised: July 19, 2023
Published online:

- [1] F. Schipper, E. M. Erickson, C. Erk, J.-Y. Shin, F. F. Chesneau, D. Aurbach, *J. Electrochem. Soc.* **2016**, *164*, A6220.
- [2] H.-J. Noh, S. Youn, C. S. Yoon, Y.-K. Sun, *J. Power Sources* **2013**, *233*, 121.
- [3] X. Feng, L. Lu, M. Ouyang, J. Li, X. He, *Energy* **2016**, *115*, 194.
- [4] X. Feng, M. Ouyang, X. Liu, L. Lu, Y. Xia, X. He, *Energy Storage Mater.* **2018**, *10*, 246.
- [5] M. N. Richard, J. R. Dahn, *J. Electrochem. Soc.* **1999**, *146*, 2068.
- [6] M. N. Richard, J. R. Dahn, *J. Electrochem. Soc.* **1999**, *146*, 2078.
- [7] R. C. Shurtz, J. D. Engerer, J. C. Hewson, *J. Electrochem. Soc.* **2018**, *165*, A3878.
- [8] D. D. MacNeil, J. R. Dahn, *J. Phys. Chem. A* **2001**, *105*, 4430.
- [9] T. D. Hatchard, D. D. MacNeil, A. Basu, J. R. Dahn, *J. Electrochem. Soc.* **2001**, *148*, A755.
- [10] D. Ren, X. Liu, X. Feng, L. Lu, M. Ouyang, J. Li, X. He, *Appl. Energy* **2018**, *228*, 633.
- [11] A. Kriston, I. Adanouj, V. Ruiz, A. Pfrang, *J. Power Sources* **2019**, *435*, 226774.
- [12] R. C. Shurtz, J. D. Engerer, J. C. Hewson, *J. Electrochem. Soc.* **2018**, *165*, A3891.
- [13] E. Kwak, J.-H. Kim, S. H. Hong, K.-Y. Oh, *Int. J. Energy Res.* **2022**, *46*, 1146.
- [14] T. He, T. Zhang, S. Gadkari, Z. Wang, N. Mao, Q. Cai, *J. Cleaner Prod.* **2023**, *388*, 135980.
- [15] J. , T. Storz, F. Kößler, A. Ebel, J. Sawodny, J. , P. Gönninger, L. Overbeck, G. Lanza, M. Hagen, J. Tübke, J. , S. Paarmann, T. Wetzels, J. Mohacs, A. Altvater, S. Spiegel, J. Klemens, P. Scharfer, W. Schabel, K. Nowoseltschenko, P. Müller-Welt, K. Bause, A. Albers, D. Schall, T. Grün, M. Hiller, A. Schmidt, A. Weber, L. de Biasi, et al., in *Towards Sustainable Customization: Bridging Smart Products and Manufacturing Systems* (Eds: A.-L. Andersen, R. Andersen, T. D. Brunoe, M. S. S. Larsen, K. Nielsen, A. Napoleone, S. Kjeldgaard), Springer International Publishing, Cham **2022**, pp. 96–104, ISBN 978-3-030-90700-6.
- [16] F. Baakes, M. Lütke, M. Gerasimov, V. Laue, F. Röder, P. Balbuena, U. Krewer, *J. Power Sources* **2022**, *522*, 230881.
- [17] O. Haik, S. Ganin, G. Gershin, E. Zinigrad, B. Markovsky, D. Aurbach, I. Halalay, *J. Electrochem. Soc.* **2011**, *158*, A913.
- [18] Y.-X. Lin, Z. Liu, K. Leung, L.-Q. Chen, P. Lu, Y. Qi, *J. Power Sources* **2016**, *309*, 221.
- [19] M. Zhou, L. Zhao, S. Okada, J. Yamaki, *J. Electrochem. Soc.* **2011**, *159*, A44.
- [20] S. E. Sloop, J. K. Pugh, S. Wang, J. B. Kerr, K. Kinoshita, *Electrochem. Solid-State Lett.* **2001**, *4*, A42.
- [21] C. Forestier, S. Grugeon, C. Davoisne, A. Lecocq, G. Marlair, M. Armand, L. Sannier, S. Laruelle, *J. Power Sources* **2016**, *330*, 186.
- [22] S.-M. Bak, E. Hu, Y. Zhou, X. Yu, S. D. Senanayake, S.-J. Cho, K.-B. Kim, K. Y. Chung, X.-Q. Yang, K.-W. Nam, *ACS Appl. Mater. Interfaces* **2014**, *6*, 22594.
- [23] R. C. Shurtz, *J. Electrochem. Soc.* **2020**, *167*, 140544.
- [24] J. Lamb, C. J. Orendorff, E. P. Roth, J. Langendorf, *J. Electrochem. Soc.* **2015**, *162*, A2131.
- [25] H. Zhou, M. Parmananda, K. R. Crompton, M. P. Hladky, M. A. Dann, J. K. Ostaneck, P. P. Mukherjee, *Energy Storage Mater.* **2022**, *44*, 326.
- [26] C. Forestier, A. Lecocq, A. Zantman, S. Grugeon, L. Sannier, G. Marlair, S. Laruelle, *J. Electrochem. Soc.* **2020**, *167*, 090513.
- [27] C. Schultz, S. Vedder, B. Streipert, M. Winter, S. Nowak, *RSC Adv.* **2017**, *7*, 27853.
- [28] F. Larsson, S. Bertilsson, M. Furlani, I. Albinsson, B.-E. Mellander, *J. Power Sources* **2018**, *373*, 220.
- [29] B. Smith RJ, M. Loganathan, M. S. Shantha, *Int. J. Chem. Reactor Eng.* **2010**, *8*.
- [30] CEN, *Guidance on Inerting for the Prevention of Explosions*, CEN/TR 15281:2006, European Committee for Standardization, Brussels **2006**.
- [31] S. Goutam, A. Nikolian, J. Jaguemont, J. Smekens, N. Omar, P. Van Dan Bossche, J. Van Mierlo, *Appl. Therm. Eng.* **2017**, *126*, 796.
- [32] R. C. Shurtz, J. C. Hewson, *J. Electrochem. Soc.* **2020**, *167*, 090543.
- [33] A. Loges, S. Herberger, P. Seegert, T. Wetzels, *J. Power Sources* **2016**, *336*, 341.
- [34] P. Taheri, M. Yazdanpour, M. Bahrami, *J. Power Sources* **2013**, *243*, 280.
- [35] S. Hoelle, S. Scharner, S. Asanin, O. Hinrichsen, *J. Electrochem. Soc.* **2021**, *168*, 120515.
- [36] S. Koch, A. Fill, K. P. Birke, *J. Power Sources* **2018**, *398*, 106.
- [37] C. Essl, A. W. Golubkov, A. Fuchs, *J. Electrochem. Soc.* **2020**, *167*, 130542.
- [38] X. Yang, H. Wang, M. Li, Y. Li, C. Li, Y. Zhang, S. Chen, H. Shen, F. Qian, X. Feng, M. Ouyang, *Batteries* **2022**, *8*, 11.
- [39] A. W. Golubkov, D. Fuchs, J. Wagner, H. Wiltse, C. Stangl, G. Fauler, G. Voitic, A. Thaler, V. Hacker, *RSC Adv.* **2014**, *4*, 3633.
- [40] C. Heubner, A. Nickol, J. Seeba, S. Reuber, N. Junker, M. Wolter, M. Schneider, A. Michaelis, *J. Power Sources* **2019**, *419*, 119.
- [41] M. Singh, J. Kaiser, H. Hahn, *Batteries* **2016**, *2*, 4.
- [42] A. Schmidt, D. Oehler, A. Weber, T. Wetzels, E. Ivers-Tiffée, *Electrochim. Acta* **2021**, *393*, 139046.
- [43] A. Schmidt, *Ph.D. Thesis*, Karlsruhe Institute of Technology (KIT), **2022**.
- [44] M. M. Ghahremanpour, P. J. Van Maaren, J. C. Ditz, R. Lindh, D. Van der Spoel, *J. Chem. Phys.* **2016**, *145*, 114305.
- [45] K. Gavritchev, G. Sharpataya, A. Smagin, E. Malyi, V. Matyukha, *J. Therm. Anal. Calorim.* **2003**, *73*, 71.
- [46] G. K. Johnson, R. T. Grow, W. N. Hubbard, *J. Chem. Thermodyn.* **1975**, *7*, 781.
- [47] Nist chemistry webbook database, <https://webbook.nist.gov/cgi/> (accessed: June 2022).